ACS APPLIED MATERIALS & INTERFACES

RESEARCH ARTICLE

www.acsami.org

SnO_2 Nanorod-Planted Graphite: An Effective Nanostructure Configuration for Reversible Lithium Ion Storage

Jong Guk Kim, Sang Hoon Nam, Sang Ho Lee, Sung Mook Choi, and Won Bae Kim*

School of Materials Science and Engineering, Gwangju Institute of Science and Technology (GIST), 261 Cheomdan-gwagiro, Buk-gu, Gwangju 500-712, South Korea

Supporting Information

ABSTRACT: We report a novel architecture of SnO_2 nanorod-planted graphite particles for an efficient Li ion storage material that can be prepared by a simple catalyst-assisted hydrothermal process. Rectangular-shaped SnO_2 nanorods are highly crystalline with a tetragonal rutile phase and distributed uniformly over the surface of micrometer-sized graphite particles. In addition, the size dimensions of grown SnO_2 nanorods can be controlled by varying the synthesis conditions. The diameter can be engineered to a sub-100 nm range, and the length can be controlled to up to several hundred nanometers. Significantly, the SnO_2 nanorod-planted graphite demonstrates an initial Li ion storage capacity of about 1010 mAh g^{-1} during the first cycle. Also, these SnO_2−graphite composites show high Coulombic efficiency and cycle stability in comparison with SnO_2 nanomaterials that are not combined with graphite. The enhanced electrochemical properties of SnO_2 nanorod-planted graphite, as compared with bare SnO_2 materials, inspire better design of composite materials with effective nanostructural configurations for advanced electrodes in lithium ion batteries.

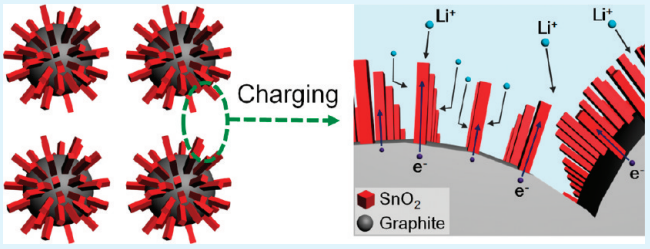

KEYWORDS: SnO_2 nanorods, graphite, anode, hydrothermal process, lithium ion batteries

INTRODUCTION

Various metal oxides, such as Co_3O_4,[1,2] CuO,[3,4] NiO,[5,6] Fe_3O_4,[7,8] and SnO_2,[9,10] have been extensively exploited as alternative electrode materials in lithium ion batteries (LIBs) because of their high energy density and relatively low cost. Among them SnO_2-based materials have attracted great interest as promising substitutes for current commercial graphite anodes because of their low cost, safety, and high theoretical lithium storage capacity (about 781 mAh g^{-1}) as compared to that of conventional graphite (about 372 mAh g^{-1}).[11,12] However, practical implementation of SnO_2 materials is still hindered by poor cyclability originating from serious volume expansion (by approximately 250% or larger) during charge/discharge processes.[13,14]

In this regard, two typical approaches have attempted to solve this problem. One is to make SnO_2 materials into effective nanostructures.[15−17] In particular, one-dimensional (1-D) SnO_2 nanostructures, such as nanowires, nanotubes, and nanorods, have been considered as powerful candidates.[18−23] For example, Park et al.[13] synthesized 1-D SnO_2 nanowires and obtained higher lithium storage (about 1134 mAh g^{-1} for the first cycle) and smaller capacity fading (1.45% per cycle). Wang and Lee[24] reported 1-D SnO_2 nanorods with high initial capacity (about 1100 mAh g^{-1}) and stable capacity retention in a relatively low potential window. Unfortunately, however, aggregation between nanomaterials often occurs, which is an issue in the use of nanostructured materials as electrodes.[2,25] Furthermore, large irreversible side reactions arising from the high surface area of nanomaterials diminish their Coulombic efficiency and energy density.[8,26] To solve these issues, another strategy is proposed, which is the synthesis of composites for the uniform dispersion of SnO_2 nanoparticles into a buffering matrix.[27,28] Because carbonaceous materials as buffers have high electrical conductivities, good mechanical properties, and reversible capacity retentions,[15−17] SnO_2 composites with carbonaceous materials may gain a considerable advantage. To this end, Wang and Lee[29] reported SnO_2−graphite composites that showed better capacity retentions than bare nanoscale SnO_2. As the SnO_2 nanoparticles are pinned on the graphite surface, the agglomeration issue could be prevented effectively, although it seems that the amount of loaded SnO_2 is probably limited to the nanoparticle population over the graphite surface. Therefore, if length-controllable SnO_2 nanorods are distributed and supported on the graphite surface, this novel construction could improve the electrode performance in the following ways: (i) Proper spacing between grown SnO_2 nanorods could enhance the wetting properties of electrolytes and accommodate deformation stress during charge/discharge.[18,22] (ii) Ductile graphitic carbon as a buffer matrix could enhance electron transfer and maintain the integrity of the electrode.[15−17] (iii) The composites could have stable cyclability at relatively high current rates from an intense affinity[30] between SnO_2 nanorods and graphite caused by heat treatments.

In this research, we report a novel composite structure fashioned of 1-D SnO_2 nanorods that are supported on graphite

Received: November 27, 2010
Accepted: February 3, 2011
Published: February 23, 2011

Scheme 1. Illustration of (a) Activated Graphite, (b) SnO_2-Seeded Graphite, and (c) SnO_2 Nanorod-Planted Graphite[a]

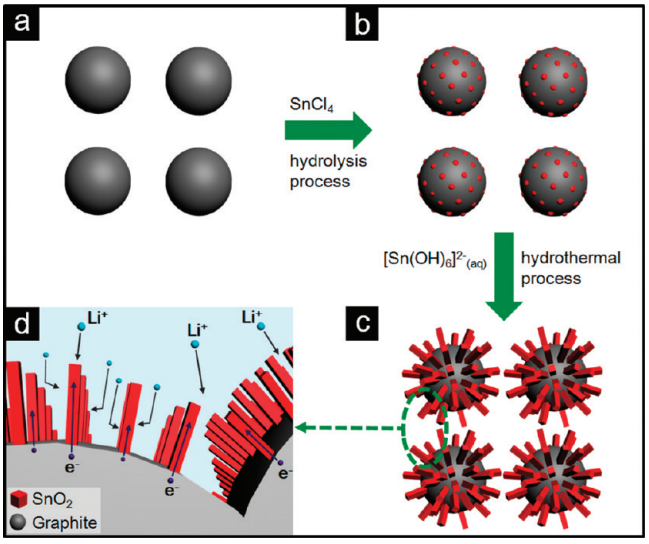

[a] In step I, colloidal SnO_2 nanoparticles are seeded onto the surface of activated graphite. In step II, SnO_2 nanorods are grown on the SnO_2 seeded-graphite surface by a hydrothermal process. (d) Illustration of electrochemical reactions (i.e., charging process) over the SnO_2 nanorod-planted graphite during cycling. This shows enhancement of Li^+ transport between SnO_2 nanorods with optimized spacing and electron conduction between SnO_2 nanorods and graphite.

microspheres, in which the SnO_2 nanorod arrays uniformly stand throughout the graphite surface and can be synthesized in a controlled manner with respect to their diameter and length by a simple hydrothermal process. Accordingly, in this work, we prepared a series of SnO_2 nanorod-planted graphite with controlled morphology in terms of the different diameters and lengths of the SnO_2 nanorods. Note that this kind of nanostructure configuration has hardly been reported in battery electrodes. More interestingly, the synthesized SnO_2 nanorod-planted graphite shows excellent initial discharge capacity and high Coulombic efficiency as compared to that of bare nanosized SnO_2. With their novel structural configuration, these SnO_2 nanorod-planted graphite materials can become promising electrode materials in overcoming the current limitations of LIB performance.

EXPERIMENTAL DETAILS

Preparation of SnO_2-Seeded Graphite. Graphite powders (Carbonix Co., average diameter = 20 μm) were stirred in an acid solution of HNO_3 (70%, Aldrich) and HCl (37%, Aldrich) (1:3 v/v) for 12 h to activate the graphite surface. The activated graphite powders were then washed with distilled water (18.2 MΩcm) and dried by the vacuum freeze-drying method. The SnO_2 nanoparticles were seeded onto the activated graphite surface by a simple hydrolysis process of $SnCl_4$ with NaOH. In a typical synthesis, the activated graphite powders (0.5 g) were dispersed in 4.1 mL of a 0.054 M aqueous $SnCl_4 \cdot 5H_2O$ (98%, Aldrich) solution. A 0.106 M NaOH (99.99%, Aldrich) aqueous solution (4.1 mL) was then added dropwise to this mixture under vigorous stirring. Precipitated colloidal SnO_2 nanoparticles were produced and subsequently deposited onto the activated graphite surface during stirring. After 12 h of magnetic stirring, the SnO_2-seeded graphite powders were rinsed several times with distilled water and ethanol, followed by drying in a convection oven at 70 °C. The dried powders were heat treated at 400 °C for 2 h under an argon atmosphere.

Growth of SnO_2 Nanorods on the SnO_2-Seeded Graphite Surface. First, a tin precursor solution was prepared in a Teflon inlet of an autoclave by mixing 0.075 mol NaOH (99.99%, Aldrich) into 50 mL of a 0.1 M aqueous $SnCl_4 \cdot 5H_2O$ (98%, Aldrich) solution. This solution was magnetically stirred for 20 min under atmospheric conditions, resulting in a transparent homogeneous solution. After adding the previously prepared SnO_2-seeded graphite (0.1 g) to this tin precursor solution, the mixture was hydrothermally heated to 200 °C and maintained at this temperature for 24−72 h. The average diameter and length of the produced SnO_2 nanorods on the graphite ranged from 28 to 37 nm and from 123 to 352 nm, respectively, depending on the growth time. The resulting material was rinsed thoroughly with distilled water and ethanol and dried in a convection oven at 70 °C. Other samples were also synthesized for different SnO_2 nanorod dimensions by changing the solution concentration to 50 mL of a 0.2 M aqueous $SnCl_4 \cdot 5H_2O$ solution and 0.105 mol of NaOH. The average diameter and length of the SnO_2 nanorods, in this case, could range from 62 to 84 nm and from 409 to 646 nm, respectively.

For the purpose of comparing with other nanostructures, SnO_2 nanowires and nanoparticles were also separately synthesized. The SnO_2 nanowires were synthesized over Au catalysts in a vapor−liquid−solid growth mechanism through a chemical vapor deposition process. These SnO_2 nanowires had a diameter around 80 nm and a micrometer-scale length.[31] The SnO_2 nanoparticles with diameters around 100 nm were synthesized by a hydrothermal process of 50 mL of a 0.01 M aqueous $SnCl_4 \cdot 5H_2O$ solution containing 6.7 mmol NaOH at 200 °C for 24 h.[14]

Physicochemical Characterization and Electrochemical Analysis. Scanning electron microscopy (SEM) measurements were conducted with a JEOL JSM-7500F. The X-ray diffraction (XRD) patterns were recorded on a powder sample with a Rigaku Rotalflex RU-200B diffractometer using a Cu Kα (λ = 1.5418 Å) source with a Ni filter at 40 kV, 40 mA, and scan rate of 0.02° s^{-1}. Transmission electron microscopy (TEM) and high-resolution TEM (HRTEM) observations were carried out with JEOL JEM-2100 operated at 200 kV. The SnO_2 contents (wt %) were determined by thermogravimetric analysis (TGA; TA Instruments, TGA 2050) with a heating rate of 10 °C min^{-1} in air.

The SnO_2 nanorod-planted graphite, carbon black, carboxyl methyl cellulose, and styrene butadiene rubber (Carbonix Co.) were mixed in a weight ratio of 80:10:5:5. The obtained slurry was pasted onto a pure copper foil using the doctor blade method to prepare the electrode, followed by drying in a vacuum oven at 145 °C for 3 h. The electrolyte was 1 M $LiPF_6$ in a 1:1 v/v mixture of ethylene carbonate and diethyl carbonate (Cheil Industries). Pure lithium foil was used as a counter electrode. Cellgard 2400 was used as a separator film. The cell (CR2032 coin type) was assembled in an argon-filled glovebox, where the concentrations of moisture and oxygen were maintained below 1 ppm. Cyclic voltammograms (CVs) were performed at a scan rate of 0.05 mV s^{-1} from 2.5 and 0.01 V with an AMETEK Solartron analytical 1400. The fabricated cells were also galvanostatically cycled at a rate of 72 mA g^{-1} between 0.01 and 1.5 V on a WBCS 3000 battery tester (WonA Tech). Electrochemical impedance spectroscopy (EIS) measurements were recorded using the multi-impedance test system after the first cycle. The frequency range was from 100 kHz to 10 mHz with AC amplitude of 5 mV.

RESULTS AND DISCUSSION

Scheme 1 presents the synthesis for SnO_2 nanorod formation on a graphite surface together with a hypothetical description of the electrochemical charging process over the prepared materials.

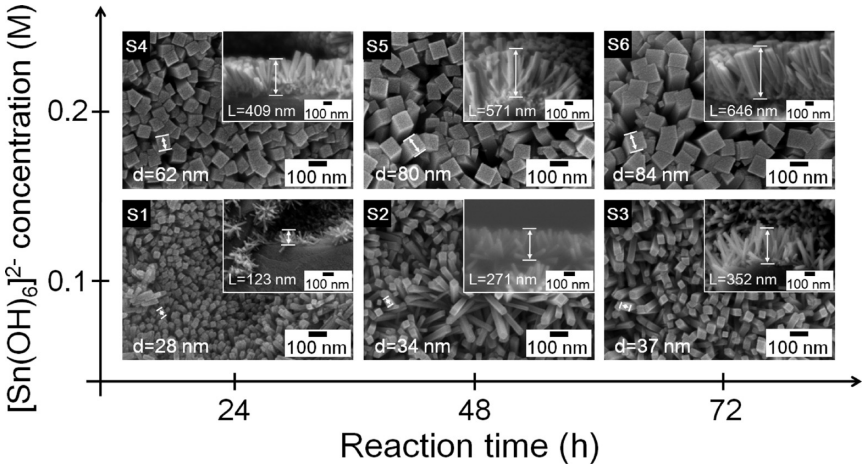

Figure 1. Typical SEM images of nanostructure evolution of the as-obtained SnO_2 nanorod-planted graphite materials (with cross-sectional images in the insets) as a function of $[Sn(OH)_6]^{2-}$ concentration and reaction time.

In the first step, SnO_2 seed particles are coated on the activated graphite surface by hydrolysis of tin(IV) chloride pentahydrate (Scheme 1b). Note that uniformly dispersed SnO_2 nanoparticles are observed on the graphite surface, and the particles make intimate contact with graphite by heat treatments (Figure S1 of the Supporting Information). This SnO_2 seed deposition is crucial for the catalytic growth of SnO_2 nanorods because it is less possible to grow nanorods without the SnO_2 seed layers. In the second step, SnO_2 nanorods are vertically grown from the SnO_2-seeded graphite surface by a hydrothermal reaction in an aqueous $[Sn(OH)_6]^{2-}$ solution (Scheme 1c). More important, both the diameter and length of the SnO_2 nanorods can be readily engineered by varying the solution concentration and reaction time, as is demonstrated in Figure 1. The conceptual electrochemical reactions for Li^+ insertion (i.e., charging process) over the SnO_2 nanorod-planted graphite are illustrated in panel (d) of Scheme 1. In short, Li^+ migrates readily into the interval spaces between the standing nanorods and then penetrates the SnO_2 nanorods (and/or graphite), which provide relatively short diffusion lengths of Li^+ due to the structural feature of the standing SnO_2 nanorods. Electrons may also be transferred effectively in this structure as the highly conductive graphite[29] allows easy electron transport to occur through the 1-D SnO_2 nanorods. This kind of SnO_2−graphite configuration can significantly improve the performance of LIBs as follows: (i) SnO_2 nanorods separately stand on the graphite support with proper interspacing, enabling electrolyte permeability to increase for faster Li^+ migration.[14,22] (ii) Because SnO_2 nanorods are firmly bonded[25,30] (i.e., planted) to the graphite surface, disintegration of the SnO_2 nanorods from graphite could be prevented. (iii) The high electric conductivity of graphite could enhance electron transfer, and ductile graphite acts as a buffer zone to mitigate mechanical stress during charge/discharge processes.[15−17,29] (iv) The decline of undesirable side reactions involving electrolyte decomposition on the graphite surface[8] could increase Coulombic efficiency as compared with that of a bare SnO_2 electrode.

Figure 1 shows SEM images of SnO_2 nanorod-planted graphite materials prepared here with different diameters and lengths of the SnO_2 nanorods. The SnO_2 nanorods are rectangular in shape and are densely distributed throughout the graphite surface. The growth of SnO_2 nanorods occurs according to the following reactions[32,33]

$$Sn^{4+} + 4OH^- \rightarrow Sn(OH)_4 \quad (1)$$

$$Sn(OH)_4 + 2OH^- \rightarrow [Sn(OH)_6]^{2-} \quad (2)$$

$$[Sn(OH)_6]^{2-} \rightarrow SnO_2 + 2H_2O + 2OH^- \quad (3)$$

The produced $Sn(OH)_4$ in eq 1 is dissolved by the presence of excess OH^- anions to form the $[Sn(OH)_6]^{2-}$ complex in eq 2. These $[Sn(OH)_6]^{2-}$ complex species are subsequently converted into SnO_2 by a hydrothermal process according to eq 3. To obtain rectangular SnO_2 nanorods, the $[Sn(OH)_6]^{2-}$ concentration and molar ratio of $SnCl_4 \cdot 5H_2O$ to NaOH play a crucial role.[34] We have observed that an appropriate $[Sn(OH)_6]^{2-}$ concentration is above 0.05 M for SnO_2 nanorod growth, and a suitable molar ratio of $SnCl_4 \cdot 5H_2O$ to NaOH is around 1:10.5−1:24 for the successful synthesis of SnO_2 nanorod-planted graphite. We have investigated the effects of the $[Sn(OH)_6]^{2-}$ concentration and reaction time on the morphology of synthesized SnO_2 nanorod-planted graphite, as shown in Figure 1 (The samples are denoted as S1, S2, S3, S4, S5, and S6 under the specified synthesis condition.). It is important to note that the average diameter of prepared SnO_2 nanorods was engineered from 28 to 84 nm, and the length could be controlled from 123 to 646 nm. With a larger $[Sn(OH)_6]^{2-}$ concentration, larger diameter and longer nanorods were obtained. When the $[Sn(OH)_6]^{2-}$ concentration was below 0.1 M, for example, 0.05 M, the SnO_2 nanorods were not produced after 24 h but were produced after 48 h (Figure S2 of the Supporting Information).

The XRD patterns (Figure 2a) indicate that the SnO_2 nanorods consist of the tetragonal rutile phase (a = 4.755 Å, c = 3.184 Å), which was confirmed by a comparison with standard values (a = 4.738 Å, c = 3.187 Å, JCPDS 41-1445). The graphite includes hexagonal (a = 2.47 Å, c = 6.79 Å, JCPDS 75-1621) and rhombohedral phases (a = 3.635 Å, JCPDS 75-2078). There is no notable peak shift or intensity variation induced by secondary phases or impurities. With increasing SnO_2 nanorod sizes, the peak intensity ratio of SnO_2 to graphite increases, implying that the weight fraction of SnO_2 increases as the diffraction intensity is proportional to the weight fractions in the composites.[35,36] More important, the relative intensity of the (002) crystal plane of

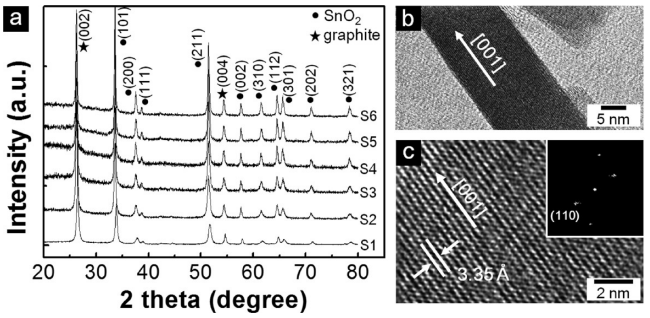

Figure 2. (a) XRD patterns of SnO_2 nanorod-planted graphite synthesized under different conditions. (b) TEM and (c) HRTEM image of separated SnO_2 nanorods. The inset in panel (c) is a corresponding fast Fourier transform pattern of the HRTEM image.

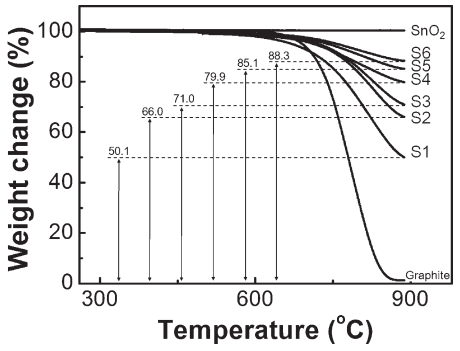

Figure 3. TGA curves of the SnO_2 nanorod-planted graphite synthesized under different conditions. The measurements were performed from room temperature to 900 °C at a heating rate of 10 °C min^{-1} in air. No weight loss was observed in the SnO_2 nanoparticles, but almost all of the graphite mass was lost.

SnO_2 also increases from S1 to S6, which means that the preferential growth direction of the SnO_2 nanorods is along the ⟨001⟩ direction. TEM and HRTEM images (Figure 2b, c) confirm the high crystallinity of the SnO_2 nanorods. The fast Fourier transform pattern (inset of Figure 2) taken from a section of a SnO_2 nanorod also reveals the single-crystal characteristics of the SnO_2 nanorods. The spacing of 3.35 Å between adjacent planes corresponds to the distance between two (110) planes of the rutile SnO_2 phase. The SnO_2 nanorod is enclosed by the (110) crystal facets, and the (001) plane is perpendicular to the nanorod axis, indicating that the growth was accelerated in the [001] direction.[37] This ⟨001⟩ preferential growth direction is also reflected in the high diffraction intensity of the (002) peaks in panel (a) of Figure 2.

The SnO_2 contents (wt %) in the obtained SnO_2 nanorod-planted graphite were quantitatively measured by TGA under an air atmosphere. The temperature was scanned from room temperature to 900 °C at a heating rate of 10 °C min^{-1}. While no weight change was observed in the SnO_2 alone, a weight change of 98.8% in graphite was observed between 600 and 900 °C. From these TGA measurements, the SnO_2 contents of as-prepared SnO_2 nanorod-planted graphite were able to be measured: 50.1, 66.0, 71.0, 79.9, 85.1, and 88.3 wt % for S1 to S6, respectively, as shown in Figure 3.

The electrochemical properties of SnO_2 nanorod-planted graphite were investigated by CVs, galvanostatic charge/discharge, and EIS measurements. Figure 4 shows the CVs of

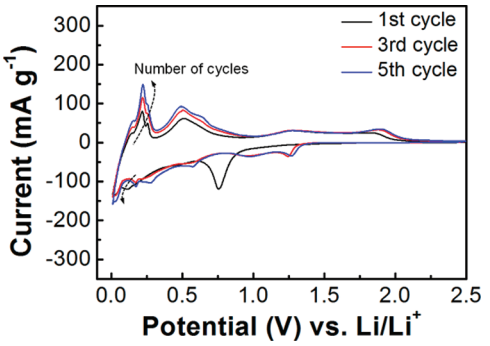

Figure 4. CVs of SnO_2 nanorod-planted graphite (S1) between 2.5 and 0.01 V at a scan rate of 0.05 mV s^{-1}.

sample S1 at a scan rate of 0.05 mV s^{-1} in the potential range of 2.5−0.01 V. The behavior of the CVs represents electrochemical reactions caused from both graphite and SnO_2 during cycling.[38,39] The following equations describe such electrochemical reactions with Li^+ ions over SnO_2 and graphite in LIBs[40]

$$4Li^+ + 4e^- + SnO_2 \rightarrow 2Li_2O + Sn \quad (4)$$

$$xLi^+ + xe^- + Sn \leftrightarrow Li_xSn\ (0 \le x \le 4.4) \quad (5)$$

$$Li^+ + e^- + C_6 \leftrightarrow LiC_6 \quad (6)$$

The CVs show a strong cathodic peak around 0.75 V that occurs from the reduction of SnO_2 (to Sn and Li_2O) and the formation of a solid electrolyte interphase (SEI) layer during the first discharge cycle, like eq 4. Moreover, relatively weak peaks are observed between about 0.7 and 0.2 V, which are related to the formation of Li_xSn according to eq 5. The peaks near 0 V are ascribed to Li intercalation into graphite to form LiC_6 by eq 6.[41] In the anodic curve, the peaks at 0.2 and 0.5 V can be attributed to Li deintercalation from LiC_6 and Li dealloying from Li_xSn, respectively. This result suggests that the charge/discharge of the composites is a stepwise process: first, Li alloys with Sn, and then Li is inserted into graphite for cathodic processes, while Li deintercalation from LiC_6 occurs first and then dealloying of Li_xSn for anodic reactions. Although the electrochemical reaction of eq 4 is known to be irreversible, it can be partially reversible when the Li_2O exists in form of a nanosized structure.[15,42] Accordingly, the cathodic peak at around 1.25 V is attributed by the formation of nanosized Li_2O, and the anodic peak at around 1.8 V appears from the decomposition of Li_2O after subsequent cycles.[15,42] Remarkably, there is an obvious increase in current density in the CV loops as the cycle increases, which indicates that there might be an activation process during the initial charge/discharge cycles.[43,44] Because the lithiation/delithiation processes cause structural modifications of electroactive materials, the activation process could be related to a reconstruction of the internal crystal structure of the SnO_2 nanorod-planted graphite. Consequently, the activation characteristics[45] are established by the Li^+ transfer rate or LiC_6 and $Li_{4.4}Sn$ formation rates. In this regard, the kinetic barriers eventually lead to gradual activation during each cycle, and the current density increases continuously until degradation dominates activation. As the activation process overwhelms degradation during the initial five cycles, the performance deterioration of the SnO_2 nanorod-planted graphite could be less severe as

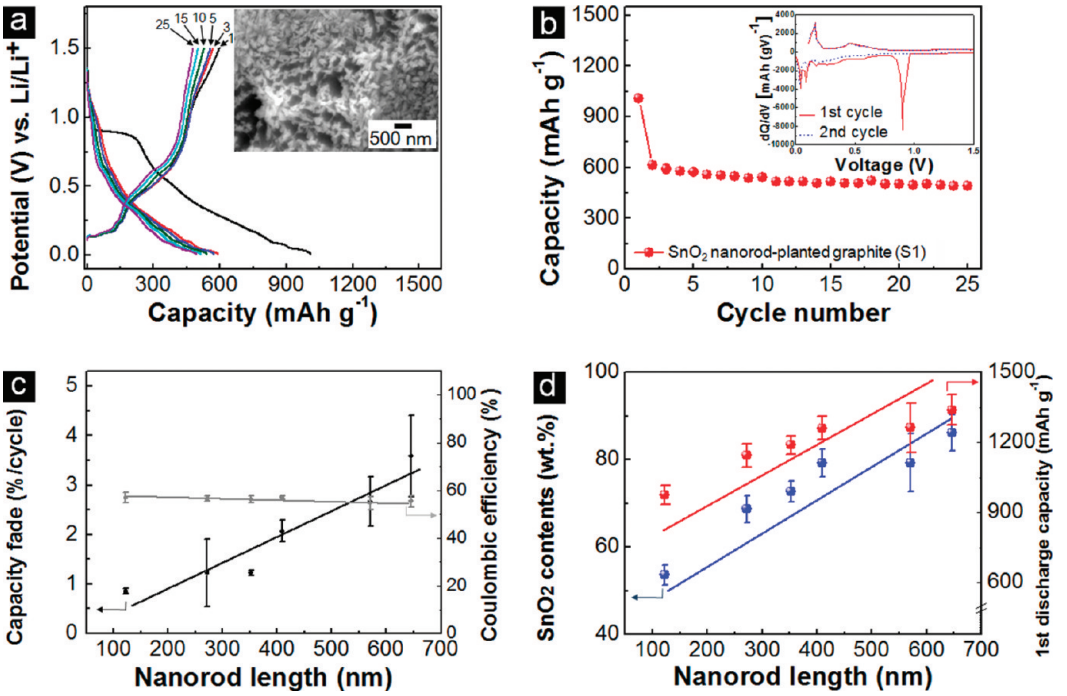

Figure 5. (a) Voltage profiles of SnO_2 nanorod-planted graphite (S1) at a current density of 72 mA g^{-1} between 0.01 and 1.5 V. The inset shows an SEM image of SnO_2 nanorod arrays after cycling 25 times. (b) Capacity cycle number curves of as-obtained SnO_2 nanorod-planted graphite (S1). The inset shows the differential capacity versus voltage plot. (c) Relations of the capacity fade and Coulombic efficiency with the nanorod length of SnO_2 nanorod-planted graphite samples S1−S6. (d) Relations of the SnO_2 contents and first discharge capacity over the different nanorod length of SnO_2 nanorod-planted graphite samples S1−S6. Here, the error limits of all the samples were determined statistically from the galvanostatic charge/discharge measurements.

compared to the cases with SnO_2 nanowires alone. (See the detailed descriptions in the Experimental Details and Figure S3 of the Supporting Information).

Panel (a) of Figure 5 shows the voltage profiles of SnO_2 nanorod-planted graphite (S1), which was cycled at a current density of 72 mA g^{-1} in the potential range of 0.01−1.5 V (versus Li/Li^+) up to 25 cycles. It is surprising to observe that SnO_2 nanorod-planted graphite delivers a very high initial discharge capacity of about 1010 mAh g^{-1}, and this capacity value is between that of SnO_2 and graphite. This higher capacity could be attributed to the 1-D SnO_2, which provides efficient electron transport and large interfacial area, thus improving kinetic properties.[13,24] In addition, stable capacity retention after the first cycle represents homogeneous dispersion of electroactive composites in the electrode film without aggregation. Note that the SnO_2 nanorod-planted graphite composite electrode shows higher initial Coulombic efficiency (59.2%) than the theoretical value (52%) for the SnO_2 electrode under full Li alloying/dealloying.[46] It is also higher than many other reports of SnO_2-based materials, whose Coulombic efficiencies typically range from 40 to 50%.[13,47] The initial irreversible capacity loss is mainly originated from electrolyte decomposition on electroactive materials. As irreversible side reactions are suppressed on carbon compared with other materials, such as Si, Fe_2O_3 and Co_3O_4,[1,48,49] SnO_2 nanorod-graphite composites could have a higher Coulombic efficiency. After the first discharge process, the SEI films covering the surface of SnO_2 nanorod-planted graphite hinder the electrolyte from being further decomposed. As a result, the Coulombic efficiency increases to 94.2% in the second cycle. The inset SEM image shows the preserved SnO_2 nanorod arrays on the graphite core after 25 cycles. In spite of volume variations, nanorod arrays maintained their structural integrity, which indicates that the loss of electrical contact with the SnO_2 nanorods has declined. Panel (b) of Figure 5 displays the galvanostatic cycling profiles of a SnO_2 nanorod-planted graphite (S1) electrode, which exhibits enhanced cycling performance and maintains a reversible capacity over 25 cycles.

The average capacity fading of SnO_2 nanorod-planted graphite is observed to be 0.85% per cycle after the second cycle, showing good capacity retention as shown in panel (c) of Figure 5. It is much smaller than the previously reported values of SnO_2 nanoparticles, nanowires, and nanorods, when they were used alone in the anode system.[13,29,47] The elasticity of carbon is larger than that of SnO_2;[50] therefore, the elastic graphite with interspacing between nanorods can accommodate strain energy effectively when SnO_2 nanorods and graphite react with Li^+. For this reason, SnO_2 nanorod-planted graphite shows a good cyclability. Nonetheless, when the composites have excessively dense SnO_2 nanorod arrays, such as S5 or S6, the performance is worse compared with composites having sparsely grown SnO_2 nanorod arrays, like S1. Limited space between nanorods might lead to poor performance, which is related to a lack of electrolyte permeability and strain relaxation. Panel (d) of Figure 5 shows that the first discharge capacity increases as the SnO_2 nanorod length increases. The SnO_2 contents inferred from the theoretical capacity values ($2Li_2O$ and $Li_{4.4}Sn$: 1494 mAh g^{-1}; LiC_6: 372 mAh g^{-1}) at the first discharge capacity are in accordance with the previous TGA measurements, implying that both SnO_2 nanorods and graphite contribute to the total capacity of the electrode (See Table S1 of the Supporting Information for details).

We further investigated the rate performances with the samples S1, S3, and S5. As shown in Figure 6, the cell was cycled

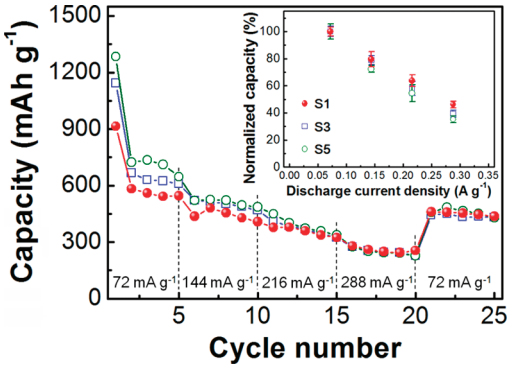

Figure 6. Cycling performance at various current densities between 0.01 and 1.5 V of SnO_2 nanorod-planted graphite (S1, S3, and S5). The inset shows the normalized capacity at each step by the average capacity values under 0.72 mA g^{-1} current density of the first step.

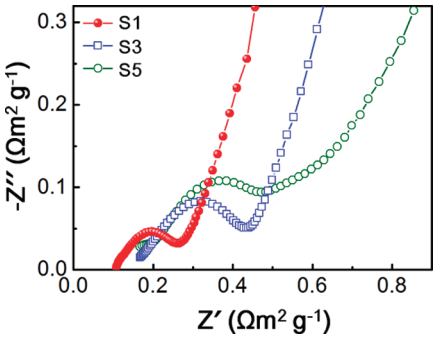

Figure 7. Nyquist plots of SnO_2 nanorod-planted graphite (S1, S3, and S5) measured at the open circuit voltage of 1.5 V.

from a current density of 72 with a stepwise increment of 72 up to 288 mA g^{-1}. Even at a high current density of 288 mA g^{-1}, the S1 is still able to deliver a substantial amount of capacity of 257.7 mAh g^{-1}. For the S3 and S5 cases, the delivered capacity was 249.3 and 248.2 mAh g^{-1}, respectively. Interestingly, when the current density was reduced back from 288 to 72 mA g^{-1}, 81.7% of the initial capacity was recovered again for S1. To elucidate the origins of the improved performance of SnO_2 nanorod-planted graphite, we also compared the rate capability of individual SnO_2 nanowires and nanoparticles under identical test conditions. The synthesized SnO_2 nanowires have diameters of around 80 nm and micrometer-sized length, and SnO_2 nanoparticles have diameters of about 100 nm. The SnO_2 nanowires and nanoparticles deliver discharge capacities of 242.5 and 192.9 mAh g^{-1}, respectively, at a current density of 288 mA g^{-1}, and the recovered capacity ratios are 58.8 and 34.4%, respectively (Figure S4 of the Supporting Information). It is noted that the normalized capacity of SnO_2 nanowires (81.8%) is higher than that of SnO_2 nanorod-planted graphite (S1, 79.5%) at a low current density of 144 mA g^{-1}, but the capacity retention of SnO_2 nanorod-planted graphite (S1, 46.2%) is improved significantly compared to that of the SnO_2 nanowires (34.5%) at a high current density of 288 mA g^{-1} (Figure S4 of the Supporting Information). Therefore, as the current rate increased, capacity fading of SnO_2 nanorod-planted graphite decreased compared to that of the SnO_2 nanowires. Excellent rate performance is demonstrated for SnO_2 nanorod-planted graphite (S1, S3, and S5) compared with SnO_2 nanoparticles and nanowires, showing stable capacity retention and a higher recovered capacity ratio. This remarkable enhancement is a clear demonstration that 1-D SnO_2 combined with graphite can improve the rate capability of SnO_2-based electrodes.

To further understand the underlying reasons for the advanced cyclability of SnO_2 nanorod-planted graphite, EIS measurements were performed after the first cycle. The Nyquist plots of S1, S3, and S5 are presented in Figure 7. The Nyquist plots consist of partially overlapped semicircles at high-to-medium frequencies and a straight line at low frequencies.[51−53] The high-frequency semicircle is related to the resistance of the SEI layer (R_{SEI}) from the passivation reaction between the electrode surface and the electrolyte.[51] The medium-frequency semicircle corresponds to charge transfer resistance (R_{ct}) at the interface between electroactive materials and the electrolyte, and the low-frequency straight line is the Warburg impedance (W_d) due to Li^+ diffusion in the electrode material. From the Nyquist plots, the diameter of the semicircle increases as the size dimensions of SnO_2 nanorods increase. These results may be related to their surface area, as the amount of electrolyte decomposition is proportional to the electrode−electrolyte contact areas.[51−53] It is also observed that the first (R_{SEI}) and second semicircles (R_{ct}) of SnO_2 nanorod-planted graphite are much smaller than those of SnO_2 nanowires and nanoparticles (Figure S5 of the Supporting Information). A considerable reduction in the sum of R_{SEI} and R_{ct} from 2.38 for SnO_2 nanowires and 1.19 for nanoparticles to 0.26 Ωm^2 g^{-1} for SnO_2 nanorod-planted graphite (S1) indicates enhanced electrical conductivity arising from composites of 1-D SnO_2 with graphite. It also shows that SnO_2 nanorod-planted graphite has higher Li^+ transfer rates from thinner SEI films compared to those of SnO_2 nanowires and nanoparticles. Accordingly, SnO_2 nanorod-planted graphite shows enhanced rate performance and cycle stability compared to SnO_2 nanowires and nanoparticles at rather high current rates.

The results so far show that SnO_2 nanorod-planted graphite has a larger capacity than graphite, and higher Coulombic efficiency and rate capability in comparison with SnO_2-based materials. The excellent performance of SnO_2 nanorod-planted graphite could be based on its unique structure, and thus, the benefits of this novel architecture could be as follow: (i) Poor cyclability of SnO_2-based materials is due to significant volume variations during charge/discharge, which results in pulverization of electrodes. The vertically standing 1-D SnO_2 nanorods and elastic graphite are believed to reduce the mechanical stress caused by rapid volume changes and, thus, alleviate electrode degradation. (ii) A high affinity between SnO_2 nanorods and graphite can create homogeneous electrical interconnections in electrode films. Consequently, it prevents the aggregation or separation of SnO_2 nanorods during charge/discharge, and good capacity retention can be obtained. (iii) Graphite support improves the conductivity of the electrode, which could enhance electron transfer and decrease ohmic losses. (iv) The theoretical Coulombic efficiency of SnO_2-based materials is 52% due to the irreversible Li_2O formation under full Li alloying/dealloying. As a result of the stable SEI formation on graphite, the Coulombic efficiency of SnO_2 nanorod-planted graphite is higher than that of SnO_2-based materials, which corresponds to increase in energy density. This novel composite configurations, therefore, could hold promise of stable cyclability and excellent rate capabilities in SnO_2-based anode materials.

CONCLUSIONS

In conclusion, we have reported a novel anode material architecture based on SnO_2 nanorod-planted graphite by a

simple hydrothermal method in which the SnO_2 nanorods were uniformly distributed on the surface of graphite particles. The dimensions of SnO_2 nanorod-planted graphite were tuned successfully by adjusting the synthesis solution concentration and reaction time. When the SnO_2 nanorod-planted graphite was used as an anode in LIBs, it displayed high initial capacity (1010 mAh g^{-1}) and Coulombic efficiency (59.2%) compared with the theoretical values of graphite (372 mAh g^{-1}) and SnO_2 (52%), respectively. Remarkably, this novel anode material had a better rate capability than the SnO_2 nanowires and nanoparticles at relatively high current rates. The enhanced electrochemical properties may originate from the effectiveness of the novel nanostructure of SnO_2 nanorod-planted graphite. In other words, the grown SnO_2 nanorods with appropriate interspacing could prevent aggregation of the electroactive material and enhance the Li^+ transfer rate during cycling. The graphite, as a buffer matrix, has high electric conductivity, which can improve electron transport and the Coulombic efficiency of SnO_2-based materials.

■ ASSOCIATED CONTENT

Supporting Information. Description of the material. This material is available free of charge via the Internet at http://pubs.acs.org.

■ AUTHOR INFORMATION

Corresponding Author
*Tel.: +82-62-715-2317. Fax: +82-62-715-2304. E-mail: wbkim@gist.ac.kr.

■ ACKNOWLEDGMENT

This work was supported by National Research Foundation of Korea (NRF) grants funded by the Korea government (MEST) (R15-2008-006-03002-0 and 20100000188). Also, we appreciate Carbonix Incorporation (Korea) for the financial support.

■ REFERENCES

(1) Poizot, P.; Laruelle, S.; Grugeon, S.; Dupont, L.; Tarascon, J.-M. *Nature* **2000**, *407*, 496–499.
(2) Li, Y.; Tan, B.; Wu, Y. *Nano Lett.* **2008**, *8*, 265–270.
(3) Gao, X. P.; Bao, J. L.; Pan, G. L.; Zhu, H. Y.; Huang, P. X.; Wu, F.; Song, D. Y. *J. Phys. Chem. B* **2004**, *108*, 5547–5551.
(4) Zheng, S.-F.; Hu, J.-S.; Zhong, L.-S.; Song, W.-G.; Wan, L.-J.; Guo, Y.-G. *Chem. Mater.* **2008**, *20*, 3617–3622.
(5) Varghese, B.; Reddy, M. V.; Yanwu, Z.; Lit, C. S.; Hoong, T. C.; Rao, G. V. S.; Chowdari, B. V. R.; Wee, A. T. S.; Lim, C. T.; Sow, C.-H. *Chem. Mater.* **2008**, *20*, 3360–3367.
(6) Huang, X. H.; Tu, J. P.; Zhang, C. Q.; Xiang, J. Y. *Electrochem. Commun.* **2007**, *9*, 1180–1184.
(7) Taberna, P. L.; Mitra, S.; Poizot, P.; Simon, P.; Tarascon, J.-M. *Nat. Mater.* **2006**, *5*, 567–573.
(8) Zhang, W.-M.; Wu, X.-L.; Hu, J.-S.; Guo, Y.-G.; Wan, L.-J. *Adv. Funct. Mater.* **2008**, *18*, 3941–3946.
(9) Idota, Y.; Kubota, T.; Matsufuji, A.; Maekawa, Y.; Miyasaka, T. *Science* **1997**, *276*, 1395–1397.
(10) Lou, X. W.; Li, C. M.; Archer, L. A. *Adv. Mater.* **2009**, *21*, 2536–2539.
(11) Courtney, I. A.; Dahn, J. R. *J. Electrochem. Soc.* **1997**, *144*, 2045–2052.
(12) Courtney, I. A.; Dunlap, R. A.; Dahn, J. R. *Electrochim. Acta* **1999**, *45*, 51–58.
(13) Park, M.-S.; Wang, G.-X.; Kang, Y.-M.; Wexler, D.; Dou, S.-X.; Liu, H.-K. *Angew. Chem., Int. Ed.* **2007**, *119*, 764–767.
(14) Liu, J.; Li, Y.; Huang, X.; Ding, R.; Hu, Y.; Jiang, J.; Liao, L. *J. Mater. Chem.* **2009**, *19*, 1859–1864.
(15) Han, S.; Jang, B.; Kim, T.; Oh, S. M.; Hyeon, T. *Adv. Funct. Mater.* **2005**, *15*, 1845–1850.
(16) Wen, Z.; Wang, Q.; Zhang, Q.; Li, J. *Adv. Funct. Mater.* **2007**, *17*, 2772–2778.
(17) Zhang, H.-X.; Feng, C.; Zhai, Y.-C.; Jiang, K.-L.; Li, Q.-Q.; Fan, S.-S. *Adv. Mater.* **2009**, *21*, 2299–2304.
(18) Chan, C. K.; Zhang, X. F.; Cui, Y. *Nano Lett.* **2008**, *8*, 307–309.
(19) Nam, S. H.; Shim, H.-S.; Kim, Y.-S.; Dar, M. A.; Kim, J. G.; Kim, W. B. *ACS Appl. Mater. Interfaces* **2010**, *2*, 2046–2052.
(20) Xu, J.; Jia, C.; Cao, B.; Zhang, W. F. *Electrochim. Acta* **2007**, *52*, 8044–8047.
(21) Wang, Y.; Zeng, H. C.; Lee, J. Y. *Adv. Mater.* **2006**, *18*, 645–649.
(22) Liu, J.; Li, Y.; Ding, R.; Jiang, J.; Hu, Y.; Ji, X.; Chi, Q.; Zhu, Z.; Huang, X. *J. Phys. Chem. C* **2009**, *113*, 5336–5339.
(23) Kim, Y.-S.; Ahn, H.-J.; Nam, S. H.; Lee, S. H.; Shim, H.-S.; Kim, W. B. *Appl. Phys. Lett.* **2008**, *93*, 103104.
(24) Wang, Y.; Lee, J. Y. *J. Phys. Chem. B* **2004**, *108*, 17832–17837.
(25) Shi, L.; Li, H.; Wang, Z.; Huang, X.; Chen, L. *J. Mater. Chem.* **2001**, *11*, 1502–1505.
(26) Bruce, P. G.; Scrosati, B.; Tarascon, J.-M. *Angew. Chem., Int. Ed.* **2008**, *47*, 2930–2946.
(27) Yoon, S.; Manthiram, A. *J. Mater. Chem.* **2010**, *20*, 236–239.
(28) Chen, J. S.; Cheah, Y. L.; Chen, Y. T.; Jayaprakash, N.; Madhavi, S.; Yang, Y. H.; Lou, X. W. *J. Phys. Chem. C* **2009**, *113*, 20504–20508.
(29) Wang, Y.; Lee, J. Y. *J. Power Sources* **2005**, *144*, 220–225.
(30) Zhang, T.; Gao, J.; Fu, L. J.; Yang, L. C.; Wu, Y. P.; Wu, H. Q. *J. Mater. Chem.* **2007**, *17*, 1321–1325.
(31) Lee, S. H.; Jo, G.; Park, W.; Lee, S.; Kim, Y.-S.; Cho, B. K.; Lee, T.; Kim, W. B. *ACS Nano* **2010**, *4*, 1829–1836.
(32) Lupan, O.; Chow, L.; Chai, G.; Heinrich, H.; Park, S.; Schulte, A. *Phys. E* **2009**, *41*, 533–536.
(33) Lupan, O.; Chow, L.; Chai, G.; Schulte, A.; Park, S.; Heinrich, H. *Mater. Sci. Eng., B* **2009**, *157*, 101–104.
(34) Vayssieres, L.; Graetzel, M. *Angew. Chem., Int. Ed.* **2004**, *116*, 3752–3756.
(35) Choi, S. M.; Yoon, J. S.; Kim, H. J.; Nam, S. H.; Seo, M. H.; Kim, W. B. *Appl. Catal., A* **2009**, *359*, 136–143.
(36) Kim, H. J.; Choi, S. M.; Nam, S. H.; Seo, M. H.; Kim, W. B. *Appl. Catal., A* **2009**, *352*, 145–151.
(37) Zhang, D.-F.; Sun, L.-D.; Yin, J.-L.; Yan, C.-H. *Adv. Mater.* **2003**, *15*, 1022–1025.
(38) Li, N.; Martin, C. R.; Scrosati, B. *Electrochem. Solid State Lett.* **2000**, *3*, 316–318.
(39) Ota, H.; Sakata, Y.; Inoue, A.; Yamaguchi, S. *J. Electrochem. Soc.* **2004**, *151*, A1659–A1669.
(40) Wang, Y.; Su, F.; Lee, J. Y.; Zhao, X. S. *Chem. Mater.* **2006**, *18*, 1347–1353.
(41) Winter, M.; Besenhard, J. O.; Spahr, M. E.; Novák, P. *Adv. Mater.* **1998**, *10*, 725–763.
(42) Mao, O.; Dunlap, R. A.; Courtney, I. A.; Dahn, J. R. *J. Electrochem. Soc.* **1998**, *145*, 4195–4202.
(43) Seo, M. H.; Choi, S. M.; Kim, H. J.; Kim, J. H.; Cho, B. K.; Kim, W. B. *J. Power Sources* **2008**, *179*, 81–86.
(44) Shin, H.-C.; Corno, J. A.; Gole, J. L.; Liu, M. *J. Power Sources* **2005**, *139*, 314–320.
(45) Kim, J.; Kim, S.-W.; Gwon, H.; Yoon, W.-S.; Kang, K. *Electrochim. Acta* **2009**, *54*, 5914–5918.
(46) Huggins, R. A. *Ionics* **1997**, *3*, 245–255.
(47) Ying, Z.; Wan, Q.; Cao, H.; Song, Z. T.; Feng, S. L. *Appl. Phys. Lett.* **2005**, *87*, 113108.
(48) Hu, Y.-S.; Rezan, D.-C.; Titirici, M.-M.; Müller, J.-O.; Schlögl, R.; Antonietti, M.; Maier, J. *Angew. Chem., Int. Ed.* **2008**, *47*, 1645–1649.
(49) Reddy, M. V.; Yu, T.; Sow, C.-H.; Shen, Z. X.; Lim, C. T.; Rao, G. V. S.; Chowdari, B. V. R. *Adv. Funct. Mater.* **2007**, *17*, 2792–2799.

(50) Zhang, W.-M.; Hu, J.-S.; Guo, Y.-G.; Zheng, S.-F.; Zhong, L.-S.; Song, W.-G.; Wan, L.-J. *Adv. Mater.* **2008**, *20*, 1160–1165.
(51) He, B.-L.; Dong, B.; Li, H.-L. *Electrochem. Commun.* **2007**, *9*, 425–430.
(52) Park, M.-S.; Kang, Y.-M.; Wang, G.-X.; Dou, S.-X.; Liu, H.-K. *Adv. Funct. Mater.* **2008**, *18*, 455–461.
(53) Huggins, R. A. *Advanced batteries: Materials Science Aspects*; Springer: New York, 2009.